Deformation twinning-induced dynamic recrystallization during laser powder bed fusion

Hossein Eskandari Sabzi[a], Xiao-Hui Li[b], Chi Zhang[c], Hanwei Fu[b,*], David San-Martín[d], Pedro E.J. Rivera-Díaz-del-Castillo[a,*]

[a] *Department of Engineering, Engineering Building, Lancaster University, LA1 4YW, United Kingdom*
[b] *School of Materials Science and Engineering, Beihang University, No. 37 Xueyuan Road, Beijing, 100191, China*
[c] *Key Laboratory of Advanced Materials of Ministry of Education, School of Materials Science and Engineering, Tsinghua University, Beijing, 100084, China*
[d] *Materalia Research Group, Physical Metallurgy Department, Centro Nacional de Investigaciones Metalurgicas (CENIM-CSIC), Avda. Gregorio del Amo 8, 28040, Madrid, Spain*

A R T I C L E   I N F O

A B S T R A C T

Nanotwin formation is observed during laser powder bed fusion (LPBF) of austenitic stainless steels fabricated with various process parameters. Transmission electron microscopy was employed to reveal the nature of such twins, which are formed due to the high strain rapid solidification inherent to LPBF. Dynamic recrystallization (DRX) was also activated during LPBF, and induced by the deformation nanotwins. A thermostatistical model is proposed to determine the critical conditions for twinning-induced DRX; the model is validated with the reported experimental results. This modelling approach offers a method to microstructurally engineer austenitic stainless steels for potential applications needing high strength and ductility.

Laser powder bed fusion (LPBF) alloys are known to exhibit superior mechanical properties compared to their wrought counterparts, with 316L austenitic stainless steel (SS) being well-known for its excellent strength and ductility [1–3]. Traditionally, thermomechanical processing such as cold rolling and annealing improve mechanical properties of wrought 316L SS [4,5]. Wang *et al.*[6] showed that nanotwins produced via pre-deformation of 316L SS can provide extra nucleation sites for recrystallization, enhancing strength and ductility. Deformation nanotwins may also increase yield stress and dislocation recovery, and subsequently strain hardening [7].

The quick LPBF heating and cooling cycles induce repetitive strains, causing hot/cold working and subsequent annealing [8,9]. It follows that embedding nanotwins as precursors for recrystallization and recovery should be attainable through LPBF without post-treatment. Recently, Gao *et al.* [10] showed that compression deformation twins of a LPBFed 316L SS promoted recrystallization. However, the occurrence of dynamic recrystallization (DRX) and recovery (DRV) in as-built LPBF components has rarely been observed [8,11]. The competition between DRX and DRV leads to low-angle

grain boundaries (LAGBs) and subgrain formation, which control the yield strength of LPBF 316L SS (supplementary material, section 2). Li *et al.* [12] reported the presence of nanotwins in a LPBF-processed high entropy alloy with an intermediate stacking fault energy (SFE); and it is known that deformation nanotwins can be thermally stable up to 1000 °C for several minutes during annealing [6], making it possible to characterise them after LPBF building. In the present work, deformation twinning-induced DRX and DRV from thermal cycling is presented.

Discontinuous dynamic recrystallization (DDRX) and DRV are competing phenomena during hot deformation in low- to medium-SFE materials [13]. In DDRX, fresh dislocation-free grains form once a critical shear strain is achieved [14], but below it DRV is activated, which may lead to continuous dynamic recrystallization (CDRX) [15]. These phenomena depend on processing conditions such as strain, strain rate and temperature. Dislocation cell boundary strain energy may activate DRV and DRX [16], as modelled via the thermostatistical approach by Galindo-Nava and Rivera-Díaz-del-Castillo [14,15]; the critical shear strain to trigger DRX depends on the strain energy at the dislocation cell boundaries, $\frac{1}{2}\mu b^3$, where μ is the shear modulus and b is the magnitude of the Burgers vector. The strain energy is decreased by (1) the dislocation entropy upon grain boundary bulging, $T\Delta S$, where T is the processing temperature, and ΔS is the dislocation entropy, and (2)

* Corresponding author.
E-mail addresses: fhwcambridge@hotmail.com (H. Fu), p.rivera1@lancaster.ac.uk (P.E.J. Rivera-Díaz-del-Castillo).

Table 1
Chemical composition of the powder in wt.%.

Fe	Cr	Ni	Mo	Mn	Si	P	S	N	C	Cu
Bal.	17.75	12.75	2.38	2	0.75	0.025	0.01	0.1	0.03	0.5

Table 2
Processing parameters including laser power (P), scan speed (v), layer thickness (t) and hatch distance (h) used for LPBF processing.

Sample	Source	P (W)	v (m/s)	t (μm)	h (μm)
S1	NU	100	1	20	70
S2	SU	200	0.30	50	110
S3	SU	200	0.47	50	110
S4	SU	200	0.40	50	110

the fraction of dislocations in the cell interior moving towards the walls, $\frac{1}{k_c}T\Delta S$, where $k_c = \frac{12\pi(1-\nu)}{(2+\nu)}(1 + \frac{T\Delta S}{\mu b^3})$, and ν is the Poisson's ratio.

This work demonstrates nanotwin formation during LPBF of 316L SS promotes DRX and DRV during the rapid thermal cycling, altering the build mechanical properties. Characterisation is performed through advanced transmission electron microscopy (TEM), adopting mathematical modelling to confirm the formation of deformation twins during LPBF, and describing their role in activating DRX and DRV. To further confirm deformation twinning-induced DRX in LPBF, tensile testing on an as-built sample is shown to promote DRX even at room temperature.

Powder from Carpenter Additive Technology ($D_{90} = 38$ μm, composition in Table 1) was adopted. $3 \times 3 \times 3$ mm^3 cubes were fabricated using a Renishaw plc (UK) AM125 (Nottingham University, NU), and an AM125 (Sheffield University, SU) with laser spot sizes of 35 and 70 μm, respectively. The specimen preparation was reported in [8,17] followed by electron backscattered diffraction (EBSD) (supplementary material, Figs. SP1, SP2, and Tables SP1, SP2). NU specimen exhibited the highest density and fraction of LAGBs; therefore, flat tensile samples (dimensions reported in [8,17]) were fabricated under the processing parameters presented in Table 2. Three mm diameter disks were machined out of the samples, ground to 50 μm thickness, and thinned using Gatan 691 Ion Beam Thinner for TEM using TECNAI G20 at 200 kV. S1 was tensile tested using Instron 3382 at 10^{-4} s^{-1}. The fractured samples were characterised via scanning electron microscopy (SEM) (Tescan Mira 3 LMHP field emission) with an EBSD detector (OXFORD Instruments symmetry) at a scanning step size of 0.8 μm, and analysed using post-processing software HKL Channel 5.

Representative microstructures (Figs. 1a,b) show planar dislocation structures and stacking faults in S1 and S2. The deformation bands of higher dislocation density (Figs. 1c,e) are identified as deformation twins using selected area diffraction patterns (SADP) in Figs. 1(d,f), displaying several nanometres thickness. Before nanotwin formation, dislocation planar slip occurs reducing cross-slip, and activating deformation twinning. Nanotwins have been reported in severely plastically deformed 316L SS [18,19], but never before in as-built LPBFed structures.

Ultra-fast LPBF solidification promotes high strain rate cyclic deformation inducing a high density of deformation nanotwins (Fig. 2), similar to twin formation under shock loading face-centred cubic (FCC) materials [20,21]. There are four main mechanisms for deformation twin formation in FCC alloys [22]: (1) The Venables pole mechanism where a perfect twin structure without stacking faults will form and grow [23]; (2) the deviated pole (DP) mechanism (Cohen and Weertman [24]) where a perfect dislocation decomposes into a Frank and a Shockley partial when it meets a barrier such as a Lomer-Cottrel lock; (3) the stair-rod cross-slip mechanism (Fujita and Mori [25]) in which multiple glide, high stress

concentration and the formation of ϵ-martensite as an intermediate phase occurs; (4) the three-layer (TL) mechanism (Mahajan and Chin [26]) in which a twin may evolve if three layers of stacking faults composed of three Shockley partials grow into each other. The deformation nanotwins contain several stacking faults (Fig. 1c) displayed discontinuously, with no ϵ-martensite (EBSD in supplementary material, section 1); therefore, DP and TL are the nanotwin formation mechanisms.

Deformation nanotwins are confirmed by El-Danaf et al.[27] approach: when a critical dislocation density (ρ_c) is reached, deformation twins can nucleate and either grow or stop by obstacles such as grain boundaries. ρ_c is expressed as ρ_c^P, and ρ_c^T for DP and TL, respectively [27]:

$$\rho_c^{P/T} = \frac{(SFE)^2}{n_S^2\mu^2b_1^2} \cdot \frac{1}{(M\alpha b - n_S b_1)^2}, \quad (1)$$

where SFE is the stacking fault energy of the alloy, b_1=0.14 nm is the magnitude of the Burgers vector of the twin source, μ=74 GPa [28], M=3 is the Taylor factor, α=0.24 is a constant of the Taylor relationship, b=0.25 nm is the magnitude of the Burgers vector, and n_S is the number of Shockly partial dislocations responsible for twin formation. n_S=1 for DP and n_S=3 for TL. LPBF enables thermo-mechanical processing via thermal straining caused by expansion and contraction cycles [8], producing a residual plastic strain. Large thermal stresses due to ultra-fast solidification induce large thermal and plastic strains forming deformation twins if the SFE is appropriate. The dislocation density due to rapid solidification can be estimated via [29]:

$$\rho = \frac{(\alpha_{CTE}\Delta T)^2}{b^2}, \quad (2)$$

where α_{CTE}=20.21 $\times$ 10^{-6} K^{-1} [30] is the coefficient of thermal expansion and ΔT is the peak (T_{peak}) and the minimum temperature difference at the thermal cycle. Following [28]:

$$T_{peak} = \frac{H_n T_b}{H_n^{max}}, \quad (3)$$

where $H_n = \frac{AP}{h_s\sqrt{\pi d v D^3}}$ is the normalised enthalpy, A=0.36 [17], h_s=7.76 $\times$ 10^9 J/m^3 is the enthalpy at melting temperature, d=6 $\times$ 10^6 m^2/s is the thermal diffusivity, and D is the laser spot size; H_n represents the amount of energy transferred to the melt pool, T_b is the boiling temperature (T_b=2885 K for 316L SS) and H_n^{max}=5.5 is the maximum allowable normalised enthalpy before evaporation [17]. H_n values for all samples are listed in Table 3. TEM observations of the distance between the partial dislocations (r_{part}) allow the calculation of SFE (Table 3) [31]:

$$SFE = \frac{(2+\nu)\mu b^2}{24\pi(1-\nu)r_{part}}, \quad (4)$$

where ν=0.3. To find ΔT for the solidification thermal cycles, the thermal model presented in the supplementary material (section 3) is adopted. The relevant temperature-time profiles for all the LPBFed samples are shown in Fig. 2a, where T_m represents the melting temperature. An example of a rapid solidification cycle is circled in Fig. 2a for S1. The values of ρ_c, and the estimated ρ after

Table 3
H_n, SFE, critical dislocation density for both twinning mechanisms (P for deviated pole and T for three-layer mechanism) and the dislocation density upon rapid solidification (calculated from the solidification thermal cycle of each sample).

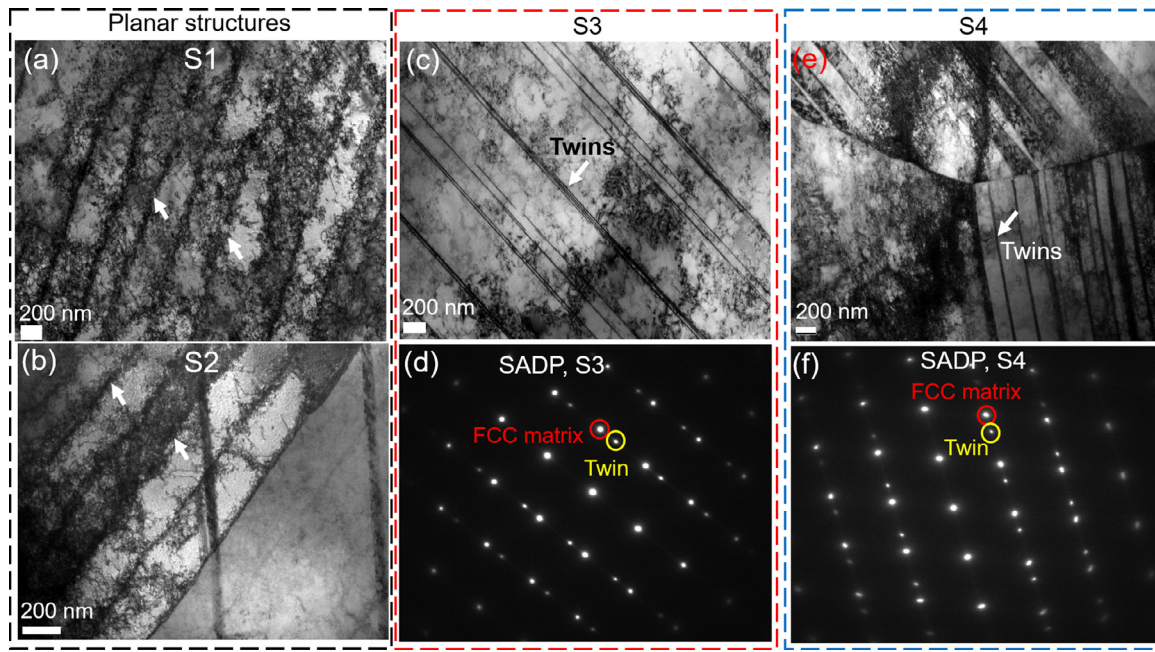| Sample	H_n	SFE (mJ/m^2)	$\rho_c^P \times 10^{14}$ (m^{-2})	$\rho_c^T \times 10^{14}$ (m^{-2})	$\rho \times 10^{14}$ (m^{-2})
1	5.1	14±5	6.5±5.2	10.5±2.4	204
2	6.6	14±5	6.5±5.2	10.5±2.4	124
3	5.3	14±5	6.5±5.2	10.5±2.4	181
4	5.7	14±5	6.5±5.2	10.5±2.4	161

Fig. 1. Bright field TEM micrographs of the as-built samples showing planar dislocation structures in (a) S1 and (b) S2 (highlighted by arrows). (c) Deformation nanotwins in S3, and (d) its corresponding nanotwins SADP. (e) Deformation nanotwins in S4, and (f) its corresponding nanotwins SADP.
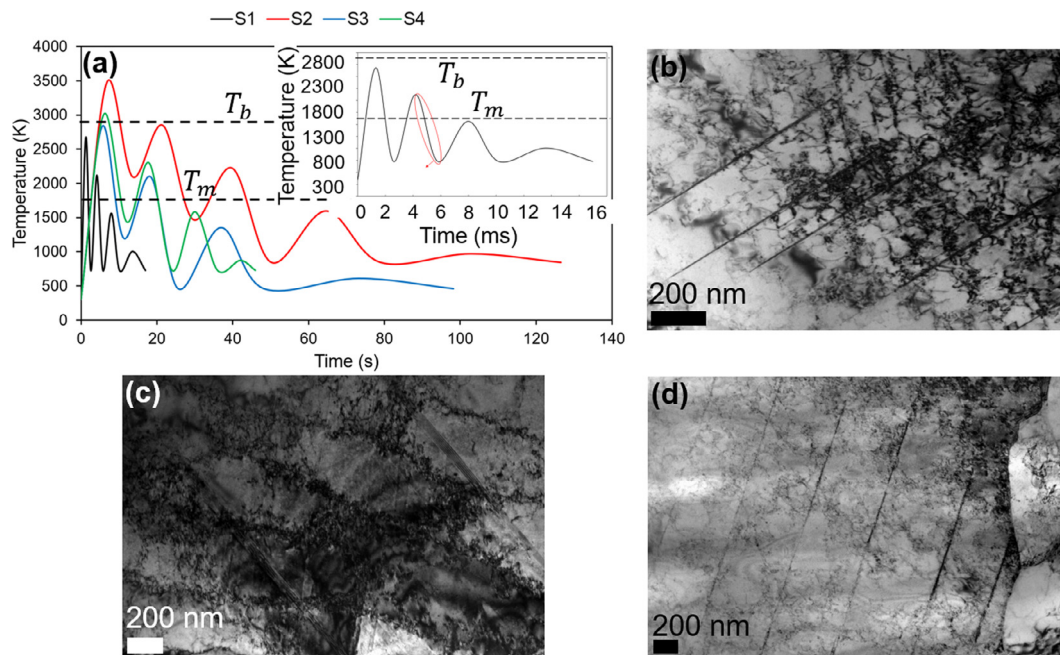

Fig. 2. (a) Temperature-time profiles for LPBF of all samples. The S1 profile is magnified in the inset, showing the rapid solidification stage with a red ellipse. (b)-(e) Bright field TEM micrographs showing the formation of nano-scale dislocation cells at the vicinity of deformation nanotwins in (b) S1, (c) S2, and (d) S3. (For interpretation of the references to colour in this figure legend, the reader is referred to the web version of this article.)

LPBF rapid solidification are listed in Table 3, showing that both DP and TL mechanisms can be activated as $\rho > \rho_c^T$ and $\rho > \rho_c^P$.

Literature reports show deformation twins can induce DRX and DRV in 316L SS [6,7,10,32]. Upon twin density saturation, shear banding accommodates strain. As the twin structure is deformed, elongated nano-scale dislocation cells can form along the shear direction (Fig. 2b-d), and further straining breaks them up into roughly equiaxed subgrains of increased misorientation, eventually evolving into randomly oriented recrystallized grains (Fig. 3) [32]. Cyclic deformation after solidification causes partial recrystallization, and deformation nanotwins are preserved unless consumed by recrystallized grains. As the thermal stability of twins is strong, and the time for their full consumption by DRX and DRV is insufficient, twins can be seen in the as-built microstructure even after numerous heating and cooling cycles. However, twin discontinuities indicate LPBF detwinning (Figs. 1c, 2 d, and 3 a), reducing dislocation density as shown by dark-field TEM images (Fig. 4), where very dark and bright regions represent areas of low (LDD) and high dislocation density (HDD). Deformation twins are not much brighter and are surrounded by LDD in the matrix.

The contribution of nanotwins to yield strengthening (σ_T) depends strongly on the dislocation mean free path and the frac-
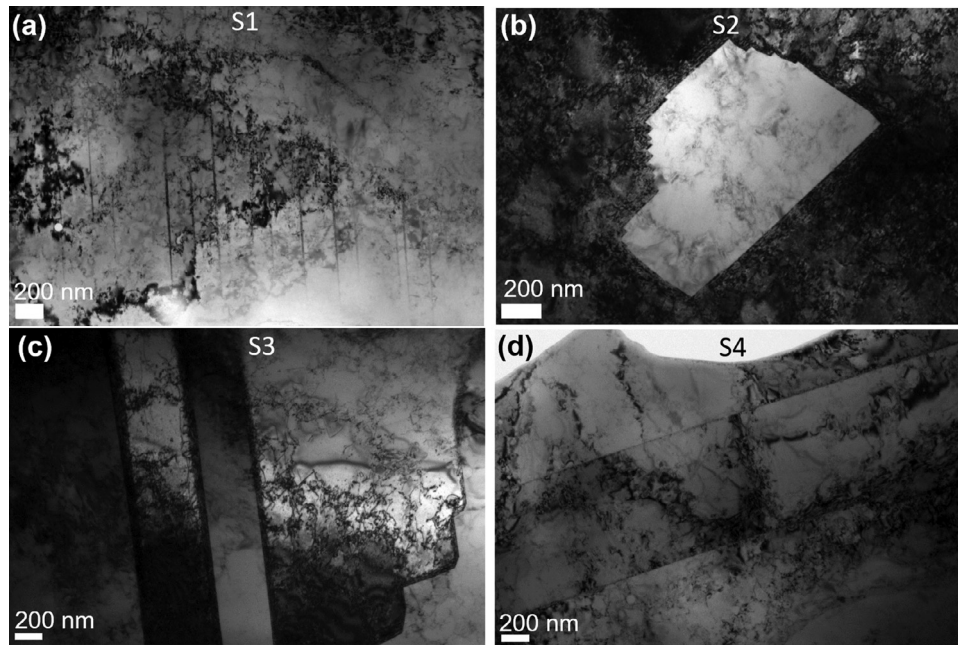
Fig. 3. Bright field TEM micrographs showing the presence of nanotwin bundles, nano-scale dislocation cells and ultrafine recrystallized grains mixed together in (a) S1, (b) S2, (c) S3, and (d) S4.
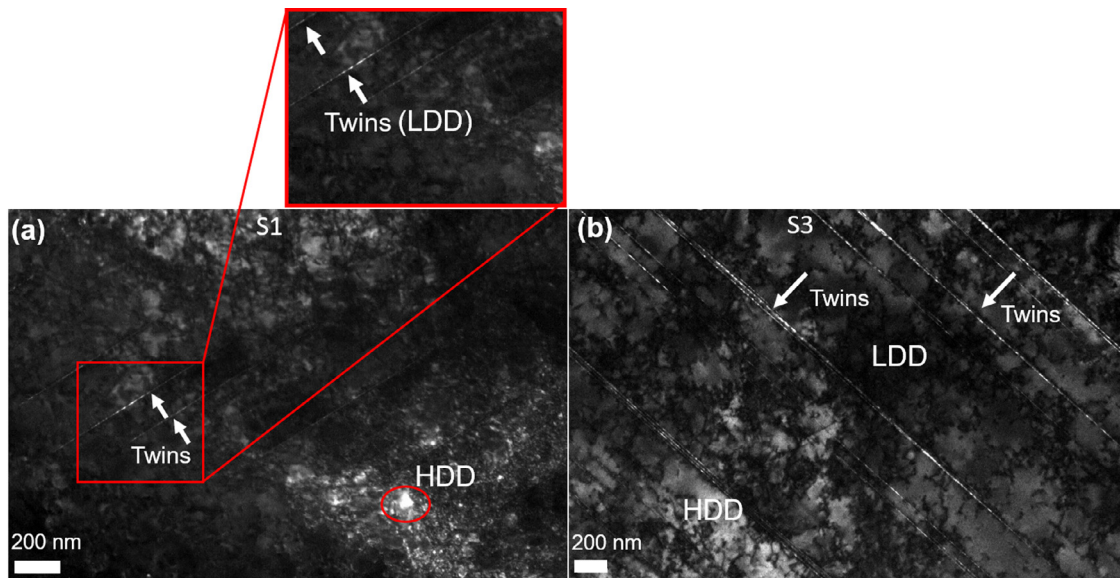

Fig. 4. Dark field TEM micrographs showing low dislocation density along the nanotwins (a) S1, (b) S3. Examples of regions with low dislocation density (LDD) and high dislocation density (HDD) are shown in the images.

tion of the nanotwins (F); $\sigma_T = M\alpha\mu b\left(\frac{1}{d} + \frac{1}{2e}\frac{F}{1-F}\right)$ [33]. A statistical study on several TEM micrographs revealed that $F < 1\%$ in all samples. Therefore, the contribution of twins depends mainly on the average grain size, d. For $d=35$ μm for S1 (EBSD, supplementary material, section 1), $\sigma_T=0.38$ MPa, which is negligible. Nevertheless, nanotwins play a vital role in the evolution of low- and high-angle grain boundaries which control yield strengthening of LPBFed 316L SS.

To quantify the possibility of twinning-induced DRX occurrence, a thermostatistical framework is developed. Considering dislocation cells as a motivator for DRX, this is triggered at a critical shear strain (γ_c^{*c}) [14]:

$$\gamma_c^{*c} = \frac{\frac{1}{2}\mu b^3 - \left(1 + \frac{1}{k_c}\right)T\Delta S}{\frac{1}{2}\mu b^3}. \tag{5}$$

But deformation twins can also act as nucleation sites for DRX [6,32]. To form deformation twins either with DP (P) or TL (T) mechanisms, a critical resolved shear stress must be overcome [34]:

$$\tau_c^{P/T} \geq \frac{SFE}{n_S b_1} + \frac{n_S\mu b_1}{L_0}, \tag{6}$$

where L_0 is the length of the twinning source, estimated here to be 200 nm [34]. Equation (1) is a sufficient but not necessary condition for twin formation. In addition to it, Eq. (6) must also be satisfied. The energy to form a deformation twin nucleus of size a can be estimated as $\tau_c^{P/T}a^3$; we assume $a=1$ nm. In order to consider only the fraction of twins that leads to bulging (necessary for DDRX), the twin energy is scaled as $\tau_c^{P/T}a^3\left(\frac{T\Delta S}{\mu b^3}\right)$. $T\Delta S$ is the dissipation entropy when grain boundary bulging oc-
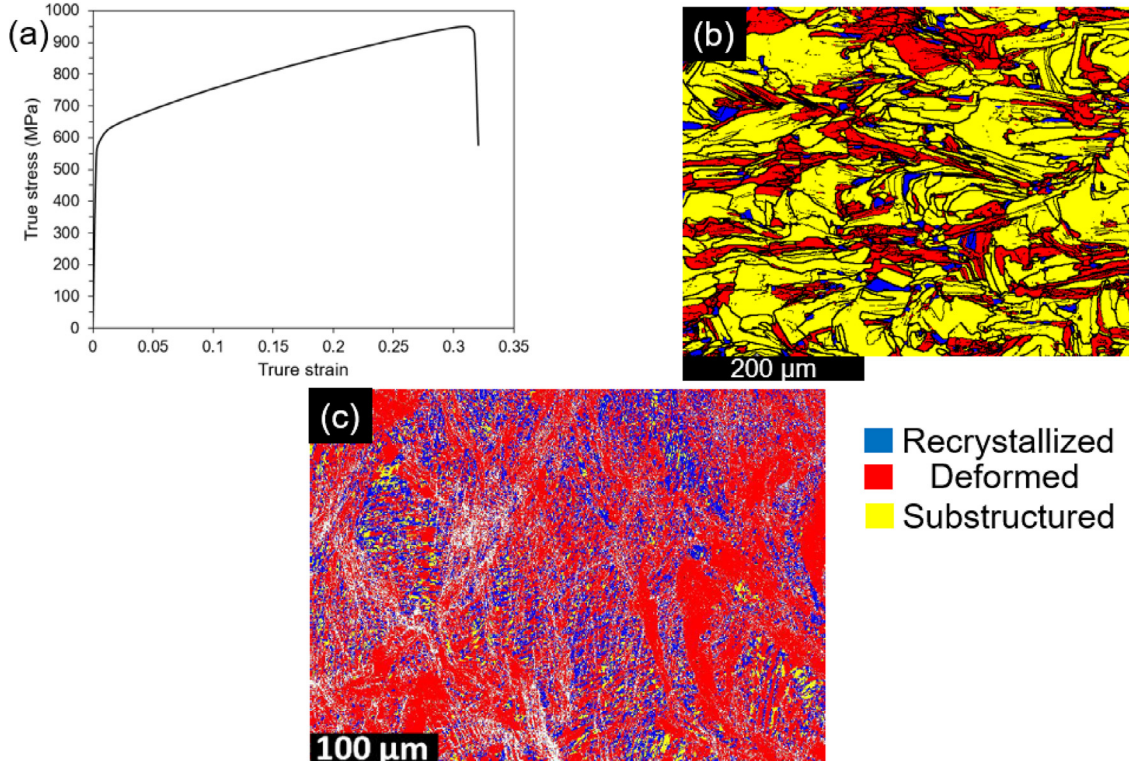
Fig. 5. (a) Tensile true stress - true strain curve of S1. Representative EBSD recrystallization map of S1 (b) prior, and (c) after tensile testing.

curs. μb^3 represents the stored energy at the grain boundaries. Hence, $\tau_c^{P/T} a^3 \left(\frac{T \Delta S}{\mu b^3} \right)$ quantifies the fraction of twins of energetically favourable conditions to activate DRX. Therefore, the critical shear strain for twinning-induced DRX (γ_c^{*t}) is:

$$\gamma_c^{*t} = \frac{\frac{1}{2}\mu b^3 - T\Delta S + \tau_c^{P/T} a^3 \left(\frac{T \Delta S}{\mu b^3} \right)}{\frac{1}{2}\mu b^3}, \qquad (7)$$

where $\Delta S = k_B \ln \left(\frac{\dot{\epsilon}_0 + \vartheta}{\dot{\epsilon}} \right)$, k_B is the Boltzmann constant, $\dot{\epsilon}_0 = cb\rho_Y$ is a constant related to the speed of sound (c=5280 m/s [35]), $\rho_Y = (0.9\sigma_Y/\mu b)^2$ is the dislocation density at the yield point, σ_Y is the yield strength (the values for yield strength are listed in Table SP3, supplementary material), $\dot{\epsilon} = \frac{k\vartheta T_{peak}}{P}$ [28] is the LPBF strain rate, with k=29 W/m·K being the average thermal conductivity of 316L SS at high temperatures [36], $\vartheta = 10^{13} \exp\left(-\frac{E_m}{RT}\right)$ is the vacancy jump frequency, E_m=73 kJ/mol [37] is the vacancy migration energy, R=8.314 J/mol·K is the universal gas constant, and T is the maximum temperature at the corresponding thermal cycle (in here restoration mechanism temperature). Using the Taylor factor $\gamma = M\epsilon$, the critical normal strain to trigger DRX from deformation twins is:

$$\epsilon_c^{*t} = \frac{\frac{1}{2}\mu b^3 - T\Delta S + \tau_c^{P/T} a^3 \left(\frac{T \Delta S}{\mu b^3} \right)}{\frac{3}{2}\mu b^3}. \qquad (8)$$

The total strain induced by LPBF (ϵ_t) processing can be divided into thermal and residual plastic strains [8]. Details for calculating ϵ_t are provided in supplementary material, section 4. The values of $\epsilon_c^{*t}(P)$, $\epsilon_c^{*t}(T)$, ϵ_t and ϵ_c^{*c} (critical normal strain for the activation of DRX via formation of dislocation cells) are listed in Table 4. ϵ_t in all samples exceeds $\epsilon_c^{*t}(P)$ and $\epsilon_c^{*t}(T)$. This demonstrates that deformation nanotwins can form after rapid solidification during LPBF, and they can trigger DRX during subsequent thermal cycles. To confirm this, tensile testing at room temperature is conducted

Table 4
Critical strain for twinning induced DRX in LPBF 316L SS. Total strain accumulated in each sample during LPBF is also reported. (P) stands for deviated pole and (T) stands for three-layer mechanism.

Sample	$\epsilon_c^{*t}(P)$	$\epsilon_c^{*t}(T)$	ϵ_t	ϵ_c^{*c}
S1	0.18±0.02	0.15±0.02	0.32	0.31
S2	0.13±0.02	0.13±0.02	0.24	0.42
S3	0.18±0.02	0.18±0.02	0.23	0.54
S4	0.12±0.02	0.13±0.02	0.23	0.26

Table 5
Fraction of deformed, recrystallized and substructured grains before and after tensile testing derived from Figs. 5(b) and 5(c).

Sample	Deformed fraction	Recrystallized fraction	substructured fraction
S1 (before deformation)	0.36	0.05	0.59
S1 (after deformation)	0.72	0.23	0.05

on S1. EBSD shows recrystallized (blue), deformed (red) and substructured (yellow) grains (Fig. 5), which fractions are shown in Table 5. Details on how the grains are categorised are outlined in supplementary material, section 1. Recrystallized grains after tensile testing increased significantly from 5% to 23%. As the critical strain for the activation of twinning-induced DRX at room temperature is 0.26±0.2 and 0.23±0.02 for DP and TL, respectively, deformation twinning triggered DRX at moderate strain levels, even at room temperature. This offers new opportunities for alloy and process design, as the critical strain for twinning-induced DRX depends on both composition-dependent properties such as shear modulus, yield strength, and SFE, as well as on process-dependent variables such as temperature and strain rate.

Alloys with a low SFE are prone to DRX. The SFE of the present alloy is 14±5 mJ/m^2, suggesting that DRX is one of the main microstructural evolution mechanisms during thermal cycling of LPBF.

DRX nucleation generally occurs at grain boundaries and deformation bands, but deformation twins can also increase its driving force. The very high dislocation densities generated at the first thermal cycles of LPBF, where rapid solidification occurs, are sufficient to generate deformation twins when the critical resolved shear for twin formation is low enough. In spite of uncertainties in SFE measurement, twin formation is still feasible. This study also proposed a new thermostatistical approach to predict the occurrence of DRX via the formation of deformation twins. This considers twin formation as the main motivator for DRX activation, instead of dislocation cell formation and DRV processes.

In summary, LPBF 316L SS samples were built with various process parameters. All the samples contained deformation nanotwins in their as-built microstructure. The nanotwins form at high strain rate solidification LPBF cycles. Deformation nanotwins assist DRX occurrence; however, as the dislocation density within the nanotwins and the nano-dislocation cells is much lower than that of subgrain boundaries, they do not contribute to the yield strength. After tensile deformation at room temperature, the fraction of DRX grains increased significantly, which is attributed to the same twinning-induced DRX mechanism. This new microstructural phenomenon recognised in LPBF of 316L SS provides a method to optimise mechanical properties by controlling both composition- and process-dependent properties.

Declaration of Competing Interest

The authors declare that they have no known competing financial interests or personal relationships that could have appeared to influence the work reported in this paper.

Acknowledgments

Supplementary material

Supplementary material associated with this article can be found, in the online version, at doi:10.1016/j.scriptamat.2021.114307

References

[1] T. Ronneberg, C.M. Davies, P.A. Hooper, Mater. Des. 189 (2020) 108481.
[2] J. Boes, A. Röttger, W. Theisen, Addit. Manuf. 32 (2020) 101081.
[3] A. Leicht, M. Rashidi, U. Klement, E. Hryha, Mater. Charact. 159 (2020) 110016.
[4] M. Eskandari, A. Najafizadeh, A. Kermanpur, Mater. Sci. Eng. A. 519 (1–2) (2009) 46–50.
[5] J. Li, B. Gao, Z. Huang, H. Zhou, Q. Mao, Y. Li, Vacuum 157 (2018) 128–135.
[6] S. Wang, T. Jozaghi, I. Karaman, R. Arroyave, Y. Chumlyakov, Mater. Sci. Eng. A. 694 (2017) 121–131.
[7] O. Bouaziz, D. Barbier, J. Nanosci. Nanotechnol. 12 (11) (2012) 8732–8734.
[8] H. Eskandari Sabzi, N.T. Aboulkhair, X. Liang, X.-H. Li, M. Simonelli, H. Fu, P.E.J. Rivera-Díaz-del Castillo, Mater. Des. (2020) 109181.
[9] M.-S. Pham, B. Dovgyy, P.A. Hooper, C.M. Gourlay, A. Piglione, Nat. Commun. 11 (1) (2020) 1–12.
[10] S. Gao, Z. Hu, M. Duchamp, P.S.R. Krishnan, S. Tekumalla, X. Song, M. Seita, Acta. Mater. 200 (2020) 366–377.
[11] N. Nadammal, S. Cabeza, T. Mishurova, T. Thiede, A. Kromm, C. Seyfert, L. Farahbod, C. Haberland, J.A. Schneider, P.D. Portella, et al., Mater. Des. 134 (2017) 139–150.
[12] R. Li, P. Niu, T. Yuan, P. Cao, C. Chen, K. Zhou, J. Alloys. Comp. 746 (2018) 125–134.
[13] K.E. Huang, R.E. Logé, Mater. Des. 111 (2016) 548–574.
[14] E. Galindo-Nava, P.E.J. Rivera-Díaz-del Castillo, Scr. Mater. 72 (2014) 1–4.
[15] E. Galindo-Nava, P.E.J. Rivera-Díaz-del Castillo, Int. J. Plast. 47 (2013) 202–221.
[16] A. Vinogradov, I. Yasnikov, H. Matsuyama, M. Uchida, Y. Kaneko, Y. Estrin, Acta. Mater. 106 (2016) 295–303.
[17] H. Eskandari Sabzi, S. Maeng, X. Liang, M. Simonelli, N.T. Aboulkhair, P.E.J. Rivera-Díaz-del Castillo, Addit. Manuf. (2020) 101360.
[18] I. Karaman, G. Yapici, Y. Chumlyakov, I. Kireeva, Mater. Sci. Eng. A. 410 (2005) 243–247.
[19] Q. Xue, X. Liao, Y. Zhu, G. Gray Iii, Mater. Sci. Eng. A. 410 (2005) 252–256.
[20] G. Krauss, Mater. Sci. Eng. A. 273 (1999) 40–57.
[21] E. Moin, L. Murr, Mater. Sci. Eng. 37 (3) (1979) 249–269.
[22] H. Idrissi, K. Renard, D. Schryvers, P. Jacques, Philos. Mag. 93 (35) (2013) 4378–4391.
[23] J. Venables, Philos. Mag. 30 (5) (1974) 1165–1169.
[24] J. Cohen, J. Weertman, Acta. Metall. 11 (8) (1963) 996–998.
[25] T. Mori, H. Fujita, Acta Metall. 28 (6) (1980) 771–776.
[26] S. Mahajan, G. Chin, Acta. Metall. 21 (10) (1973) 1353–1363.
[27] E. El-Danaf, S.R. Kalidindi, R.D. Doherty, Metall. Mater. Trans. A. 30 (5) (1999) 1223–1233.
[28] H. Eskandari Sabzi, P.E.J. Rivera-Díaz-del Castillo, Mater. Des. (2020) 109024.
[29] S. Gorsse, C. Hutchinson, M. Gouné, R. Banerjee, Sci. Technol. Adv. Mater. 18 (1) (2017) 584–610.
[30] J.-O. Andersson, T. Helander, L. Höglund, P. Shi, B. Sundman, CALPHAD 26 (2) (2002) 273–312.
[31] R.C. Reed, Cambridge University Press, 2008.
[32] G. Liu, N. Tao, K. Lu, J. Mater. Sci.Technol. 26 (4) (2010) 289–292.
[33] H. Zhi, C. Zhang, S. Antonov, H. Yu, T. Guo, Y. Su, Acta Mater. 195 (2020) 371–382.
[34] J. Huang, Y. Wu, H. Ye, Acta Mater. 44 (3) (1996) 1211–1221.
[35] L.M. Headings, K. Kotian, M.J. Dapino, Smart Materials, Adaptive Structures and Intelligent Systems, volume 56031, American Society of Mechanical Engineers, 2013. V001T04A012
[36] W. Jiang, Y. Zhang, W. Woo, Int. J. Pressure. Vessels. Piping. 92 (2012) 56–62.
[37] R.E. Smallman, R.J. Bishop, Elsevier, 1999.